Materials Science & Engineering C 128 (2021) 112298

Contents lists available at ScienceDirect

Materials Science & Engineering C

journal homepage: www.elsevier.com/locate/msec

Development of Si doped nano hydroxyapatite reinforced bilayer chitosan nanocomposite barrier membranes for guided bone regeneration

Sedef Tamburaci [a], Funda Tihminlioglu [b,*]

[a] Izmir Institute of Technology, Graduate Program of Biotechnology and Bioengineering, Gulbahçe Campus, Urla, İzmir, Turkey
[b] Izmir Institute of Technology, Department of Chemical Engineering, Gulbahçe Campus, Urla, İzmir, Turkey

ARTICLE INFO

Keywords:
Chitosan
Si doped nanohydroxyapatite
Periodontal regeneration
GBR membrane

ABSTRACT

Guided Bone Regeneration (GBR) is a widely used process for the treatment of periodontal defects to prevent the formation of surrounding soft tissue at the periodontal defect and to provide hard tissue regeneration. Recently GBR designs have focused on the development of resorbable natural polymer-based barrier membranes due to their biodegradability and excellent biocompatibility. The aim of this study is to fabricate a novel bilayer nanocomposite membrane with microporous sublayer composed of chitosan and Si doped nanohydroxyapatite particles (Si-nHap) and chitosan/PEO nanofiber upper layer. Bilayer membrane was designed to prevent epithelial and fibroblastic cell migration and growth impeding bone formation with its upper layer and to support osteogenic cell bioactivity at the defect site with its sublayer. Microporous and nanofiber layers were fabricated by using freeze-drying and electrospinning techniques respectively. The effect of Si-nHap content on the morphological, mechanical and physical properties of the composites were investigated using SEM, AFM, micro-Ct, compression test, water uptake capacity and enzymatic degradation study. Antimicrobial properties of nanocomposite membranes were investigated with tube dilution and disk diffusion methods. *In vitro* cytotoxicity of bilayer membranes was evaluated. Saos-2 and NIH/3T3 proliferation studies were carried out on each layer. *In vitro* bioactivity of Saos-2 and NIH/3T3 cells were evaluated with ALP activity and hydroxyproline content respectively. Results showed that Si-nHap incorporation enhanced the mechanical and physical properties as well as controlling biodegradability of the polymer matrix. Besides, Si-nHap loading induced the bioactivity of Saos-2 cells by enhancing cell attachment, spreading and biomineralization on the material surface. Thus, results supported that designed bilayer nanocomposite membranes can be used as a potential biomaterial for guided bone regeneration in periodontal applications.

1. Introduction

Periodontitis is a common disease which arises from chronic inflammation and induces damage on periodontal soft and hard tissues. Periodontium tissue is composed of gingiva, cementum, periodontal ligament and alveolar bone. In addition, periodontal tissues have low capacity to regenerate without a treatment. There have been different clinical treatment methods to repair the periodontal defects as soft tissue and bone replacement grafts, root surface biomodification, growth factors and barrier membranes, and their combination. Thus, recent clinical treatments have focused on extensive use of guided tissue regeneration [1–4]. Guided bone regeneration is achieved by the use of biomaterials and surgical techniques to prevent the invasion of surrounding connective tissue into the defect area. Biomaterial design for dental applications have focused on guided tissue regeneration for the treatment of periodontal diseases and healing after implantation. Especially bone grafts and barrier membranes have come into prominence as biomaterials for periodontal hard tissue regeneration [5]. Barrier membranes prevent infiltration of surrounding tissues into the bone defect. When barrier membrane is placed in direct contact with bone surface, it provides space and protects the bone defect area by eliminating soft tissue cell proliferation at the defect area. In addition, wound at the defect area can be protected from mechanical disruption and salivary contamination with the use of barrier membrane [6].

Various GBR barrier membranes have already been used in clinical practice for dental and maxillofacial applications. Membranes have been classified as resorbable (PLA, PGA, collagen, chitosan) and non-resorbable (PTFE) polymeric membranes [7]. First generation

* Corresponding author.
E-mail address: fundatihminlioglu@iyte.edu.tr (F. Tihminlioglu).

https://doi.org/10.1016/j.msec.2021.112298
Received 8 March 2021; Received in revised form 26 June 2021; Accepted 2 July 2021
Available online 7 July 2021

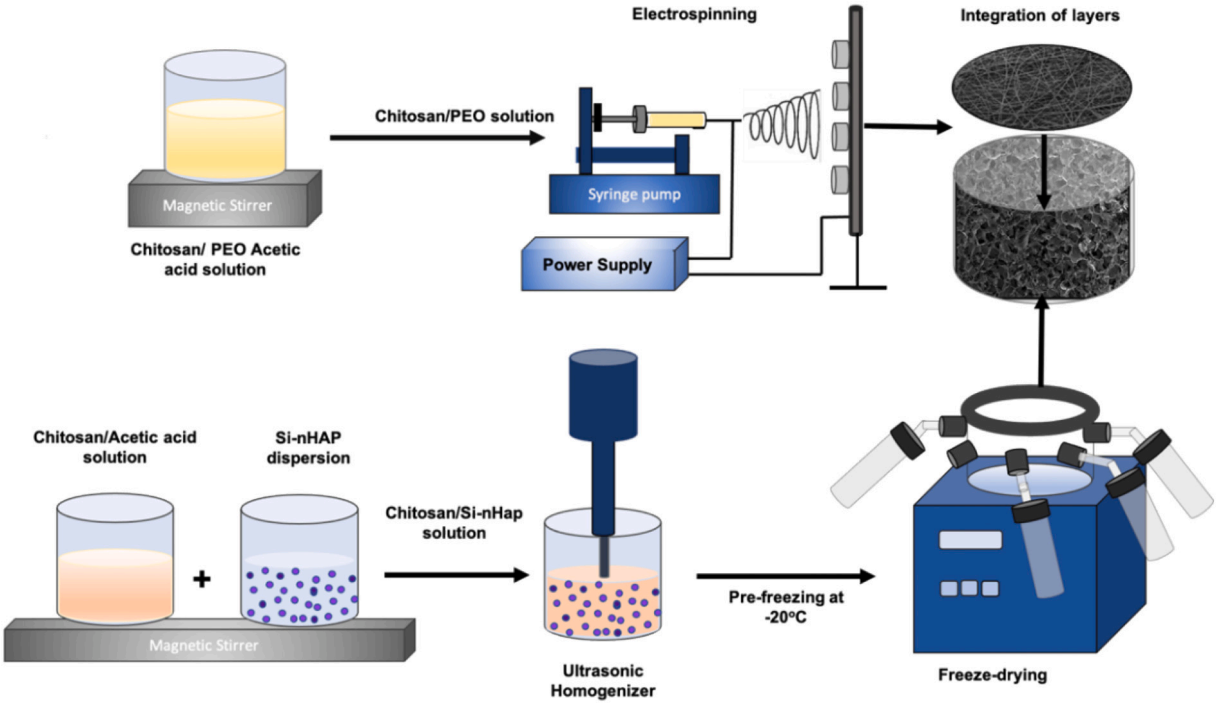

Fig. 1. Fabrication of chitosan/Si-nHap porous layer and chitosan/PEO nanofiber layer in schematic view.

membranes are designed with non-resorbable synthetic polymers, yet additional surgery need to remove the membrane causes morbidity or further possible complications such as pain and infection [8]. Thus, resorbable membranes have been used and categorized as two groups as synthetic membranes (PLLLA, PLGA *etc.*) and natural biopolymers (chitosan, collagen *etc.*) [9,10]. Generally, neat polymer structures do not meet the need of bone tissue due to the lack of structural and chemical similarity. Therefore, polymer composites have been preferred to counterbalance the inorganic content of bone tissue at the defect site. By this way, membrane designs have been improved and membrane properties have been optimized with regard to mechanical properties and degradation, host tissue integration, biocompatibility and clinical use to overcome the limitations of the current products. Therefore, recent studies have focused on composite systems to improve both the physical, barrier and bioactive properties of membranes [11–14].

Resorbable biopolymer-based membranes are especially preferred due to the fact that they provide functional tissue integration, vascularization and degradation by-products of biopolymers do not show any toxic effect leading to elimination of foreign body reaction [8,15]. Among biopolymers, chitosan is mostly used amino polysaccharide derived from chitin as its deacetylated form [16]. The use of chitosan has come into prominence due to its outstanding properties and unique characteristics as high biocompatibility, biodegradability, inherent antimicrobial activity, muco-adhesiveness and structural similarity with extracellular matrix components [17,18].

Bone tissue mainly consists of both polymer phase collagen and mineral components. Mineral phase is mainly composed of Ca, P, O and trace ions as Na^{+}, SiO_4^{4-} Mg^{2+}, SO_4^{2-}, Sr^{2+}, Ni^{2+}, F^{-} *etc.* As one of the most frequently used bone graft material, synthetic hydroxyapatite resembles the composition of mammalian hard tissue with its stoichiometric similarity of Ca/P ratio (1.67). However, it lacks the presence of beneficial trace ions in natural bone tissue. Thus, it is considered as bone graft for the inferior bone repair, but it does not accelerate the bone regeneration process. Recent hydroxyapatite designs have focused on eliminating this limitation by dopping hydroxyapatite particles with trace ions as SiO^4, Mg^{2+}, and Ni^{2+} *etc.* [19]. Silicon (Si) is an essential element for bone tissue growth and biomineralization process that it enhances the stability and bioactivity of biological apatite. The inclusion of Si ion may help to enhance the osteoblast differentiation by affecting specific gene families. Besides, Si induces the production of the bone extracellular matrix (ECM) by enhancing the prolyl 4-hydroxylase which is known as a key enzyme in biosynthesis of collagen [19–25].

Besides mimicking the chemical structure to enhance the bioactivity, the 3D morphology of GBR membranes have come into prominence and they have been improved as functionally graded materials (FGM) to mimic the hard-soft tissue interface physically [26]. Among FGM designs, GBR membrane designs have been improved especially as layered microstructures to ensure the different microenvironments for both soft and hard tissue as well as preserve the barrier property [27–29]. However, these layered designs were fabricated as compartments of similar microstructures deposited one after the other. Therefore, we designed a novel GBR membrane by integrating two biopolymer based layers which have different microstructure morphology and composition to fulfill the requirements of both soft and hard tissue at the dental defects.

In this study, it is aimed to develop a novel bilayer dental barrier membrane made up of natural polymer, *chitosan and Si-doped nanohydroxyapatite* as a nanocomposite structure. Bilayer membrane was fabricated to mimic periodontal tissue at dental defects. As the upper layer of bilayer membranes has nanofiber structure that mimics the extracellular matrix of soft tissue and acts as a barrier for fibroblast migration where the lower layer provides appropriate porous microenvironment for bone tissue regeneration inducing bioactivity with Si doped nanohydroxyapatite reinforcement. Functional barrier membrane aimed to be developed for bone defect areas in dental applications with antibacterial and resorbable properties of chitosan as well as accelerating biomineralization with Si-doped nanohydroxyapatite component. Porous lower layer was fabricated with a lyophilization method and the nanofibrous upper layer was fabricated with electrospinning method. Morphological characteristics of each layer were investigated with SEM and AFM analyses. Structure of bilayer membranes were characterized physically, and mechanically. In addition, *in vitro* bioactivity of fabricated membranes was evaluated by means of cytotoxicity, cell proliferation, attachment, ALP activity, biomineralization and hydroxyproline content.

2. Material & methods

Commercial chitosan with low and medium molecular weight powder and Polyethylene oxide (PEO-Mw 600,000) were purchased from Sigma-Aldrich and used for preparation of bilayer nanocomposites. Si doped nanohydroxyapatite (Si-nHap) (Sigma-Aldrich) was used as a bioactive reinforcement agent. Acetic acid (analytical grade, Sigma-Aldrich) was used as a solvent for preparation of nanocomposites. BCA kit (Thermo Fisher Scientific) and BSA (Bovine Serum Albumin-Aldrich, Sigma) were used for protein adsorption assay. Lysozyme (Aldrich, Sigma; from chicken egg white), sodium azide and phosphate buffer solution (10×) (Sigma-Aldrich) were used for biodegradation studies. Dulbecco's Modified Eagle medium (DMEM, SEROX), fetal bovine serum (FBS-SEROX) penicillin-streptomycin solution (SEROX) and L-glutamine (200 mM, SEROX) were used for *in vitro* cell culture studies. WST-1 assay (Biovision Inc.) was used to determine cell cytotoxicity and proliferation. ALP Assay kit (Biomerieux, Enzyline PAL Optimise) was used to determine alkaline phosphatase activity. Osteocalcin secretion was measured with Human OC/BGP (Osteocalcin) ELISA Kit (Elabscience). Paraformaldehyde (PFA, Merck) was used for cell fixation. NucBlue (DAPI) and Alexa Fluor 555 (Thermo Fisher Scientific, Molecular Probes) were used for fluorescence staining.

2.1. Fabrication of bilayer membranes

2.1.1. Preparation of chitosan/Si-nHap porous layer

Porous layer was fabricated with both low and medium molecular weight chitosan to investigate the effect of different chitosan solutions on morphology and physical properties of scaffolds. Chitosan/Si-nHap nanocomposite was prepared by separately preparing 1% *w/v* chitosan solution and Si-nHap (10, 20, 40, 50% (*w*/w)) dispersion in acetic acid (1% *v*/v). Si-nHap particles were dried in a vacuum oven overnight to remove moisture and prevent agglomeration before dispersion in acetic acid. Then chitosan solution and Si-nHap dispersion were mixed followed by a continuous stirring and sonicated with Misonix Ultrasonic Liquid Processor for 30 min (15 °C-35 Amplitude) for homogenous distribution of Si-nHap particles. Composite mixture was poured into well-plates for molding and pre-freezed at −20 °C for 24 h. After pre-freezing, samples were lyophilized at −46 °C and 0.01 mBar vacuum. Freeze dried porous scaffolds were stored in a desiccator for further use (Fig. 1).

2.1.2. Preparation of chitosan/PEO Nanofiber layer

Chitosan nanofiber layer was fabricated by electrospinning method (Fig. 1). Polyethylene oxide was used as a plasticizer in 2% *w/v* medium molecular chitosan solution. Nanofiber structure was optimized by changing voltage (15 and 20 kV), flow rate (1,2,3 ml/h), polymer/plasticizer ratio (70:30, 80:20 and 90:10), syringe diameter (17G, 21G) and acetic acid ratio (70, 80, 90%). Optimization study parameters and groups were given in a Supplementary file as Table S1.

2.1.3. Integration of chitosan/Si-nHap and chitosan/PEO layers

Fabricated Chitosan/Si-nHap porous layers were characterized and optimum Si-nHap ratio was determined for further use in bilayer structure. In addition, fiber forming solution and electrospinning parameters were chosen among the optimization groups. Then, the chitosan/PEO solution was electrospun on a chitosan/Si-nHap composite porous layer which was previously anchored on the collector of the electrospinning system with double-sided aluminum tape (Fig. 1).

2.2. Characterization

2.2.1. Scanning electron microscopy (SEM) analysis

Morphology of porous and fiber layers, integration of each layer and average thickness of bilayer membrane were observed with SEM (Quanta FEG 250) analysis. Porous and fiber layers were sputter-coated with a thin gold layer (Emitech K550X) before SEM analysis. In addition, pore wall surface structure, Si-nHap distribution on polymer surface, the effect of Si-nHap incorporation on lateral pore structure porous layer and the effects of electrospinning parameters on fiber structure were observed with SEM analysis. Average lateral pore size and fiber diameter calculations were carried out with Image J software.

2.2.2. Total surface area and porosity determination

BET surface analysis was used to determine the specific surface area of porous layers by adsorption-desorption of nitrogen. Total porosity % of porous layers were investigated with mercury porosimeter (Micromeritics, AutoPore IV) and micro-CT (Scanco-μCT 50) analyses. In addition, 3D morphology and cross sections of porous layers were observed with micro-CT analysis. Analysis was performed with native resolution at 45 kVp-88uA. Scaffolds were scanned through 500 slices using 3 μm voxel size.

2.2.3. Atomic force microscopy (AFM) analysis

Chitosan/Si-nHap composite membranes were fabricated with a solvent casting method and used to investigate the effect of Si-nHap particles on surface morphology of the chitosan matrix. AFM analysis was performed by using Nanoscope SPM (Digital Instruments Inc., USA). Point probe cantilever tip was used in tapping mode and Nanoscope software was used to determine the 3D surface morphology and roughness of membrane surfaces. Surface roughness was calculated as the root mean square average of the surface height deviations from the mean image data plane (Rq).

2.2.4. Mechanic test (compression)

Compression moduli and mechanical strength of dry CHI/Si-nHap porous layer groups were investigated with compression tests. Fabricated porous LMW and MMW CHI/Si-nHap layers were characterized with compression tests according to the ASTM D 5024-95a standards (TA XT Plus Texture Analyzer). Compression test was performed with 5 kgf load cell and 5 mm/min crosshead speed up to 75% and 90% of original height.

2.2.5. Water uptake capacity

Water uptake capacity of porous layers were determined with swelling study. Samples were incubated in 1× PBS solution for 24-48 h at 37 °C. Dry weights of porous layers were measured before incubation (Wd). Wet samples were weighed (Ww) after incubation. Swelling % of porous layers were also investigated with neutralization and without neutralization procedure. Swelling % was evaluated using Eq. (1).

$$Swelling\% = \frac{(W_w - W_d)}{W_d \times 100} \quad (1)$$

2.2.6. Protein adsorption

Protein adsorption is a major process in cell-material interaction. Adsorption of proteins in body fluids provides cell attachment and proliferation by inducing intercellular signals. In this study, protein adsorption on porous and fiber layers of bilayer membranes was determined with BCA protein assay (Thermo Fisher). Assay was performed according to microplate procedure. Bovine serum albumin (BSA) solution was used as a standard solution to calculate protein content. Samples were incubated in 0.1% (*w/v*) BSA solution at 37 °C for 24–48 h. Protein assay was performed with BCA kit according to microplate procedure.

2.2.7. Open porosity determination with liquid displacement method

Open porosity of chitosan/Si-nHap composites were measured with liquid displacement method. Specimens were immersed in a graduated cylinder with ethanol (V_1). The cylinder is then incubated in a vacuum oven at 25 °C to discharge excess air filled into the pores and provide ethanol through the pores. After vacuum, total volume in the graduated

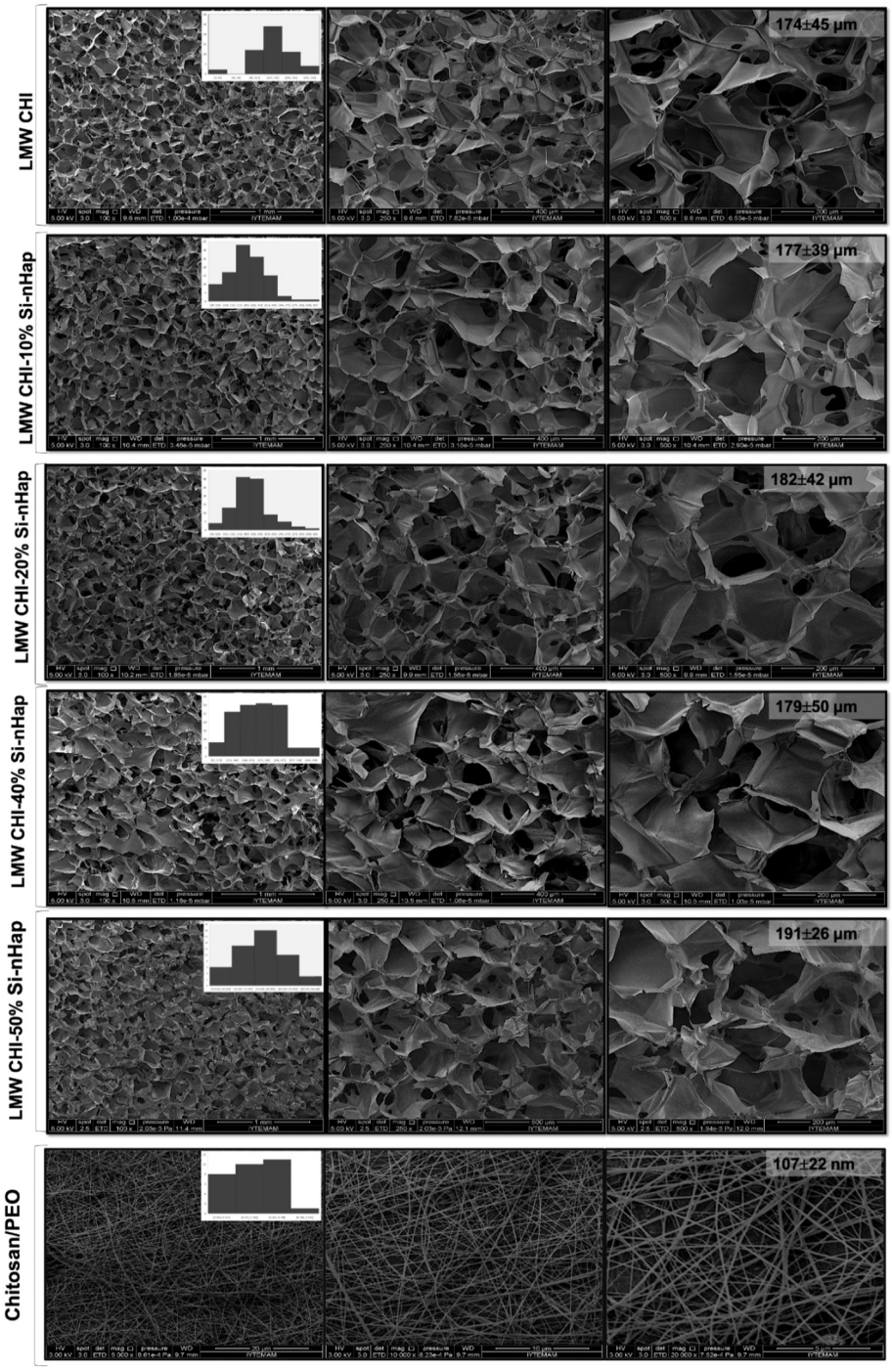

Fig. 2. SEM images of porous layer groups (bottom layer) fabricated with low molecular weight chitosan (LMW CHI) with 100×, 250× and 500× magnification and SEM images of chitosan/PEO nanofiber barrier layer (upper layer) fabricated with electrospinning method with 5000× (a),10,000× (b) and 20,000× (c) magnification respectively.

cylinder (ethanol and scaffold) is recorded as V_2. The volume difference (V_2—V_1) is calculated as the volume of the skeleton of the specimen. Finally, the scaffold is taken out, and V_3 is measured as the residual ethanol volume. The open porosity of the scaffold is evaluated with the Eq. (2).

$$\varepsilon = \frac{(V_1 - V_3)}{(V_2 - V_3)} \tag{2}$$

2.2.8. Enzymatic degradation

Enzymatic degradation of bilayer membranes was evaluated by weight loss determination. Bilayer membranes were incubated in 1× PBS solution (pH 7.4) at 37 °C with 1.5 μg/ml lysozyme to mimic the concentration in human blood serum [30]. Sodium azide (0.01%) was added to an enzymatic degradation solution to inhibit microbial contamination. Enzymatic solution was changed thrice a week to prevent the loss of enzymatic activity and to mimic the body fluid circulation in normal physiological condition. Samples were taken off from solution at 7, 21 and 28 days of incubation and dried to investigate weight change. Weight loss % was evaluated using Eq. (3) as shown below; where W_o and W_1 are dry and wet weight of the samples, respectively.

$$Weight\ Loss\% = (W_0 - W_1)/W_0 \quad (3)$$

2.3. Determination of antimicrobial activity

Antimicrobial activities of CHI/Si-nHap composites were determined by disc diffusion and tube dilution methods on *Escherichia coli* (*E. coli*) and *Staphylococcus aureus* (*S. aureus*). In the disc diffusion method, frozen stocks were activated at 37 °C for overnight. Cultured microorganisms were suspended in phosphate-buffered saline (PBS) solution and turbidity was adjusted to McFarland 0.5. Then, the swab was streaked on the Mueller-Hinton agar plates. The empty discs with 14 mm diameter were placed on the inoculated agar. 20 μl of film forming solutions (FFS) of chitosan/Si-nHap were dropped onto empty discs (Oxoid™). Amoxicillin and oxacillin antimicrobial susceptibility discs (10 $\mu g ml^{-1}$, Oxoid™) were used as positive controls. Then, plates were incubated at 37 °C for 24 h. The clear zones around the discs were measured and recorded as inhibition zones that indicate antimicrobial property. All groups were tested with three samples and average inhibition zones were calculated for each group. Similarly, activated *E. coli* and *S. aureus* stocks were cultivated in peptone water broth and adjusted to McFarland 0.5 for tube dilution method. Then bacteria (5 μl) were cultivated with broth (95 μl) and composite solution (100 μl) for 24 h at 37 °C in a spectrophotometer (Varioskan). and growth curves of bacteria were evaluated. However, Si-nHap dispersion caused turbidity and prevented us from obtaining significant absorbance measurements. Thus, at the end of the 24 h incubation period, microbial colonies in 96 well plates were cultivated in petri dishes in which tryptic soy broth/agar was poured previously. Groups were cultivated as duplicate samples. Then, the decrease in colonies was determined with counting methods.

2.4. In vitro studies

Saos-2 and NIH/3T3 cell lines were used to mimic the soft and hard tissue in periodontium. Cells were cultivated in DMEM supplemented with 2 mM L-glutamine, 10% fetal bovine serum, 100 μg/ml streptomycin and 100 U/ml penicillin in an atmosphere of 5% CO_2 at 37 °C.

2.4.1. Cell attachment and proliferation

Cell attachment and spreading on each layer of bilayer membranes were analyzed with fluorescence microscopy. Saos-2 and NIH/3T3 cells were incubated on porous and fiber layers for 3 days. Cell fixation each layer was performed by incubating layers with 3.7% paraformaldehyde (*v*/v) in PBS solution for 20 min at room temperature. Fixed cells were observed with DAPI-Alexa Fluor 555 staining to detect nuclei and cell membrane. Layers were washed with 1× PBS solution and cells were permeabilized with 0.1% Triton X-100 for 5 min before fluorescence staining. The stained cells were visualized with fluorescent microscopy.

2.4.2. ALP activity, osteocalcin secretion and hydroxyproline content

Osteogenic differentiation of Saos-2 cells was detected with ALP expression and osteocalcin secretion. Saos-2 cells on the CHI/Si-nHap composite layers were incubated with osteogenic medium (1 μl/ml L-ascorbic acid, 10 μl/ml β-glycerophosphate in complete medium) on 7, 14, 21 and 28 days of incubation. Extracellular ALP secretion of cells on the porous layer was measured spectrophotometrically (Thermolab Systems, Multiskan Spectrum) using Enzyline PAL Optimise ALP kit (Biomerioux Inc.). The measurement was performed at 405 nm according to the manufacturer's protocols. Osteocalcin (OC) secretion of Saos-2 cells cultured on CHI/Si-nHap composite layers was determined using Human OC/BGP (Osteocalcin) ELISA Kit (Elabscience). Culture media was extracted from cell incubated porous layers and analyzed for determination of the OC concentrations at 21 and 28 days of culture. Bioactivity of NIH/3 T3 cells was investigated with detection of hydroxyproline content by Hydroxyproline (Hyp) Colorimetric Assay Kit-Acid hydrolysis Method (Elabscience).

2.4.3. Biomineralization with Von Kossa and Alizarin Red S staining

Calcium and phosphate depositions on the porous layer were observed with Von Kossa (vK) and Alizarin Red S (ARS) staining. Porous layers were incubated with 3.7% paraformaldehyde (*v*/v) before staining protocol. In the von Kossa staining protocol, porous layers were stained by incubation in 1% (*w/v*) aqueous silver nitrate (Sigma-Aldrich) for 30 min under UV light. Then samples were washed with distilled water and immersed in 5% (w/v) sodium thiosulfate (Sigma-Aldrich) for 5 min to remove unreacted silver on the material surface. 2% (w/v) aqueous ARS stain (pH 4.1) was used for detection of calcium deposition on material surface. In ARS staining protocol, samples were incubated in the dark for 30 min, then rinsed with distilled water several times to remove excess stain. Stained samples were observed with a stereomicroscope (Olympus SOIF DA 0737). ARS-stained samples were incubated with acetic acid solutions to extract the stain and extracts were analyzed spectrophotometrically at 405 nm to quantify the calcium mineral deposition difference between groups.

3. Results & discussion

3.1. Fabrication and optimization of porous and fiber layers

Porous layer was fabricated using chitosan with different molecular weights and optimized with regard to the porosity, pore size and morphology. In addition, different Si-nHap concentrations were used to investigate the distribution of Si-nHap in the chitosan matrix and the effect of particle concentration in physical properties of polymer. SEM images of LMW chitosan groups were depicted as Fig. 2 and MMW chitosan groups were given as Fig. S1 in a Supplementary file. SEM images showed that LMW chitosan groups showed more uniform microstructure compared to MMW chitosan groups. Increasing molecular weight of chitosan increased the viscosity of polymer/Si-nHap solution and affected the microstructure inducing the enlargement of pore walls (Figs. 2, S1).

Chitosan-10% PEO solution (90:10) was prepared with 90% acetic acid for electrospinning process. Nanofiber layer was fabricated with 3 ml/h velocity at 20 kV and using 17G needle diameter-10 cm collector distance. The effect of PEO concentration, acetic acid %, and electrospinning parameters (voltage, distance and needle diameter) were investigated, and optimum working parameters were determined according to the SEM images of optimization groups before fabrication (Fig. S2). Groups prepared with 80% acetic acid and chitosan/PEO with 90:10 ratio formed fibers whereas, changing chitosan/PEO ratio to 70:30 led to formation of nanofibers with nano spherical beads. At 80:20 chitosan/PEO ratio with 90% acetic acid solution, uniform nanofibers were observed. SEM images of groups having different chitosan/PEO ratios with 90% acetic acid solution and constant electrospinning parameters (20 kV, 3 ml/h, 10 cm) were depicted in supplementary file as Fig. S3. At 70:30 ratio nanospheres were obtained whereas, at 80:20 ratio nanofibers were obtained with an average diameter of 340 nm. At 90:10 ratio, the average nanofiber diameter decreased to 107 nm. In literature it is indicated that successful electrospinning of chitosan solution without bead formation is generally not possible without plasticizer addition. Electrospinning of a polymer solution is subjected to the critical chain entanglement among macromolecular chains of polymer structure and the intermolecular interactions among polymer chains reduce the viscosity. PEO is the most common biologically inert plasticizer containing neutral moieties that reduces the viscosity of the chitosan solution and leads to relaxation of the chain entanglement [31,32]. Concerning to the nanofiber morphology and size, 90:10 chitosan/PEO ratio was chosen for upper layer fabrication. SEM images of groups prepared with 90% acetic acid indicated that increasing PEO ratio from 90:10 to 70:30 induced nanosphere formation due to the viscosity decrease which arises from plasticizer effect in polymer

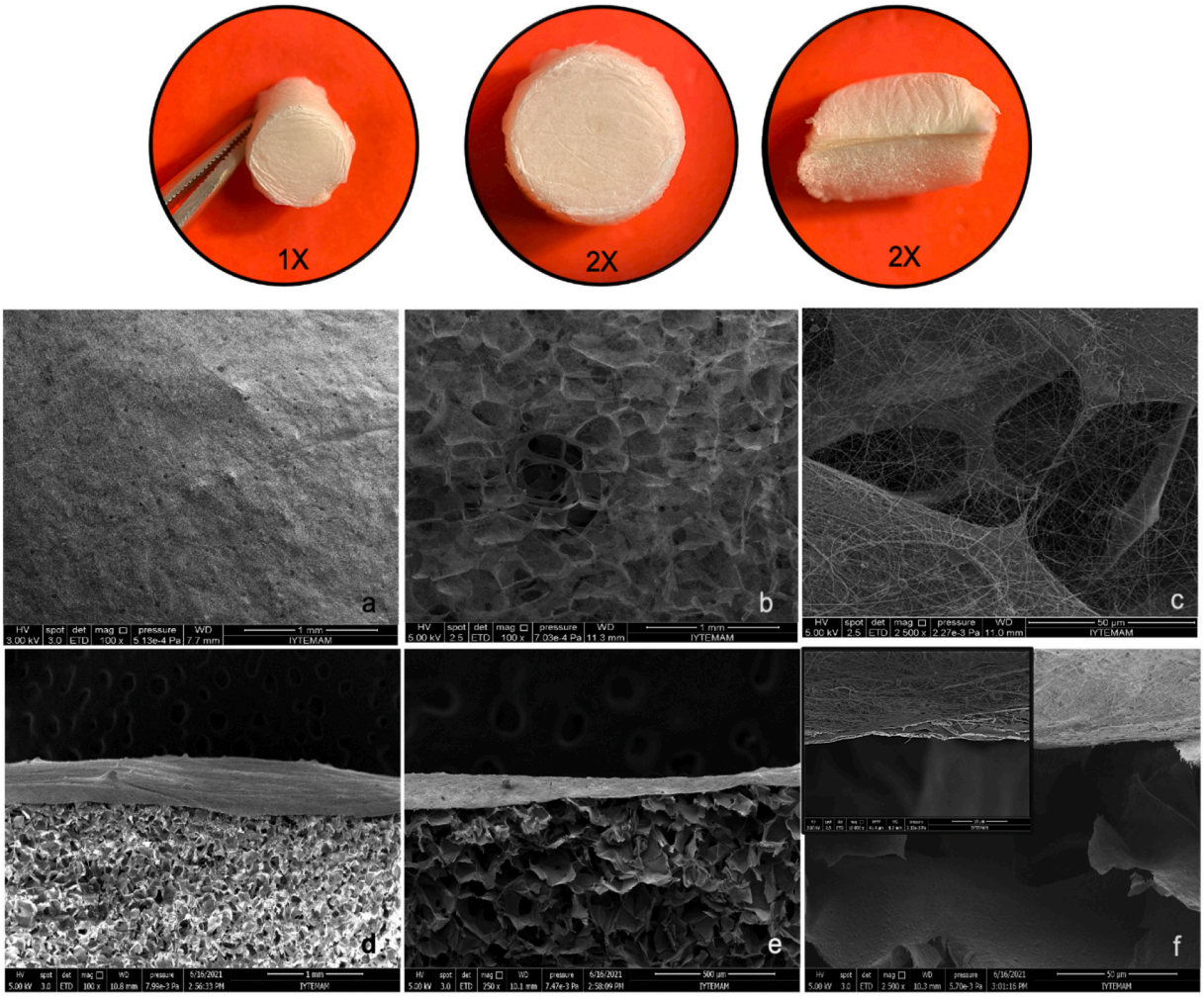

Fig. 3. Stereomicroscopy images of bilayer membranes (1×, 2×) and SEM images of chitosan/PEO nanofiber coated porous layer surface (a,b,c) with 250×, 1000× and 2500× magnifications; cross-sectional view of bilayer structure (d,e,f) with 250×, 500× and 10,000× magnifications.

solution. 70 and 80% acetic acid concentrations caused non-homogenous fiber distribution and blockage at the needle tip during the process. Thus, 90% acetic acid group was chosen for nanofiber fabrication (Fig. 2).

3.2. 3D structure, morphology and porosity

Average pore size of the barrier membrane has a significant effect on prevention of excessive fibrous tissue penetration into the defect site and at the same time to allow neovascularization and bone tissue formation [15]. In this study, the porous layer was designed to provide a favorable microenvironment for bone tissue formation whereas, nanofiber layer was designed to prevent soft tissue formation. Thus, average pore size of porous layer, average nanofiber diameter, distance between nanofibers and thickness of nanofiber layer was measured to observe whether each layer fit the purpose of guided tissue regeneration. The pore size is a significant factor in barrier membrane morphology to prevent fibroblast penetration into the defect site and excessive soft tissue formation instead of hard tissue. Besides, appropriate pore size is required to initiate vascularization for bone tissue regeneration. In literature, an appropriate pore size range for bone ingrowth is indicated as 50–100 μm to provide optimum microenvironment for cell migration, effective gas and nutrient transport. In addition, osteon formation can be observed on pores larger than 150 μm [15,33]. Results showed that all scaffold groups ensured this requirement for biological activities. In this study, SEM images indicated that LMW chitosan groups exhibited more interconnected and uniform microstructures to mimic porous morphology of trabecular bone. Average lateral pore size, pore size distributions of LMW chitosan/Si-nHap scaffold groups were depicted in Fig. 2. Average pore size of LMW chitosan scaffolds were evaluated in the range of 174–191 μm whereas MMW chitosan groups had an average pore size in the range of 252–306 μm (Table S2). However, MMW chitosan groups possessed non-homogenous microstructure and pore morphology (Fig. S1). In addition, specific surface areas of porous layers were determined with BET surface analyses and given as Table S3 in a Supplementary file. Results showed that LMW chitosan groups possessed total surface area in the range of 4.35–5.18 m^2/g whereas, MMW chitosan groups had total surface area range as 2.60–4.58 m^2/g. It is indicated that LMW chitosan groups showed higher total surface area due to having homogeneous porous interconnected microstructure.

Pore diameter of fiber layers generally changes with the fiber diameter due to the effect of fiber stack formation during the fiber deposition by electrospinning [34]. SEM images indicated that uniform chitosan/PEO nanofiber morphology was obtained for chitosan/PEO solution and average fiber size was determined as 107 ± 22 nm (Fig. 2). In literature, it is indicated that cell-material interaction is better on nanofiber structures when compared to microfiber forms. Because nanofiber morphology determines the optimum space for cell attachment and migration. The distance between each nanofiber was measured as average pore size for the nanofiber layer and found as 1.8 ± 0.5 μm. The approximate size of NIH/3T3 fibroblasts is known as 18 μm. Thus, average pore size of fabricated nanofiber layer was found

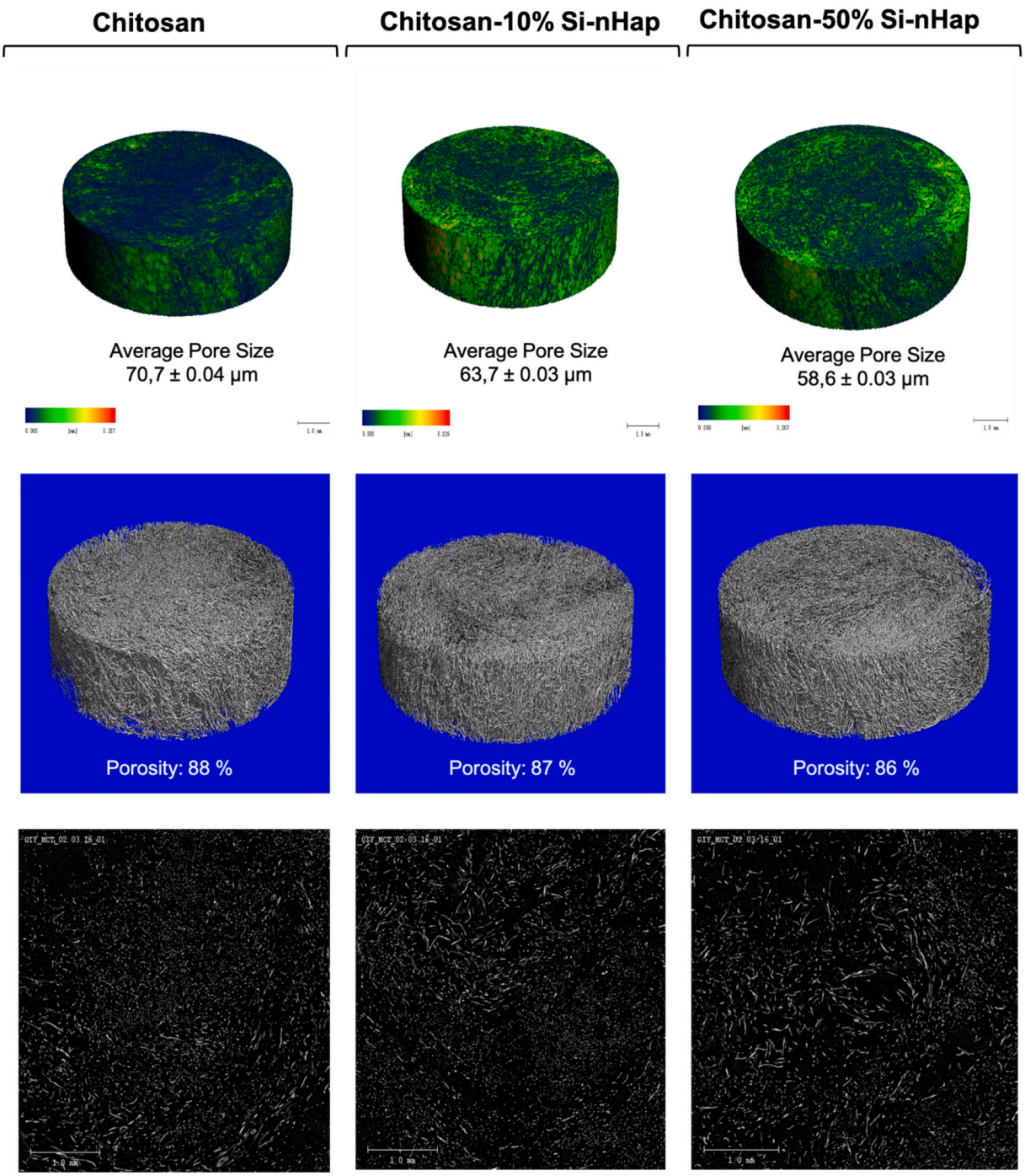

Fig. 4. Micro CT images showing 3D structure, colored pore size distribution and cross-sectional view of porous chitosan and chitosan/Si-nHap layers at 1 mm scale: Total porosity and average pore size of scaffolds were reported.

appropriate to prevent fibroblast migration through the defect site. Lowery and co-workers fabricated PCL/PEO nanofibers with different peak pore diameters and investigated the effect of the distance between nanofibers on fibroblast attachment and proliferation. Results indicated that large voids ($D > 6$ um) induced cell proliferation compared to small pore diameter ($D < 3.1$ um). However, fluorescence images showed that decreasing pore diameter led to cell attachment on the fiber mat surface instead of penetrating through the fiber layer. SEM images showed that fibroblasts could not bridge between the larger pore diameters and cells infiltrated the inner part of nanofiber layers. Besides, slow ECM production was observed between fibers that have larger pore diameters. Small pore diameters provided cell growth and branching with 3D cell morphology [35].

Nanofiber layer was integrated on a porous layer by electrospinning chitosan/PEO solution on a chitosan/Si-nHap composite porous layer which was attached to the collector of the system. Stereoimages of bilayer membranes showed that each layer was attached successfully, and uniform bilayer structure was obtained (Fig. 3). SEM images showed that two layers were integrated successfully, and a nanofiber layer formed a barrier on the top of the porous layer with an average thickness of 3.4 ± 0.36 µm (Fig. 3). In Fig. 3a, SEM image of thick nanofiber layer on the top of microporous sublayer was depicted to observe the uniformity of upper layer whereas, Fig. 3b and c shows the thinner coating of nanofiber layer to observe and prove the integration of each layer as

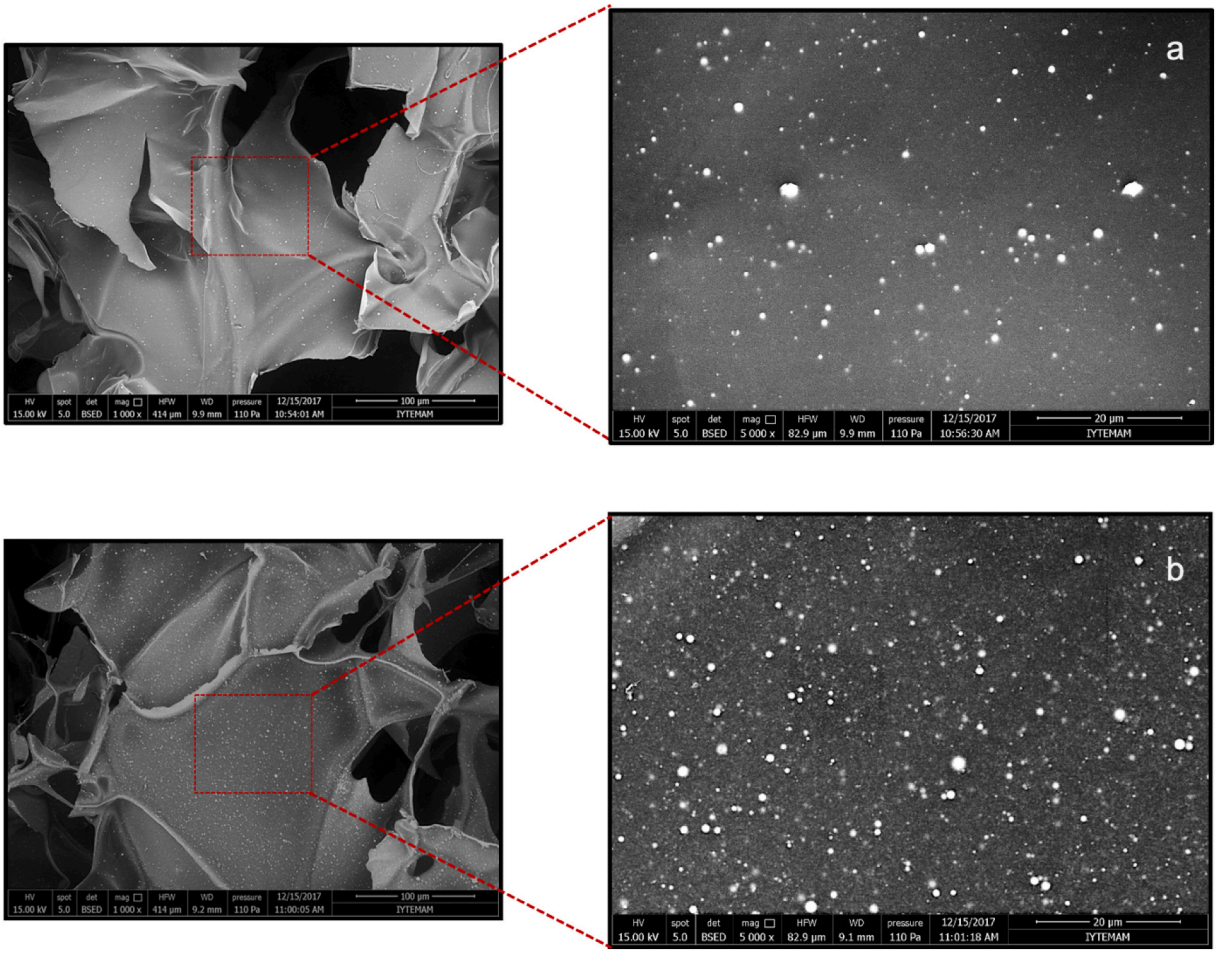

Fig. 5. SEM images show the Si-nHap distribution on pore walls of porous layer: Chitosan-10% Si-nHap (a), Chitosan-50% Si-nHap (b) with 1000× and 5000× magnifications respectively.

nanofiber-micropore interaction. 3D structures of porous chitosan and chitosan/Si-nHap layers were investigated with micro-CT analyses. Images showing 3D structure, colored pore size distribution and cross-section demonstrated that highly interconnected porous structures were obtained with a morphology composed of smaller pores at the center whereas, larger pores at the peripheral region (Fig. 4). Total porosity of chitosan scaffold was evaluated as 89% with mercury porosimeter. Chitosan/Si-nHap nanocomposites with increasing Si-nHap concentration (10–50%) possessed total porosity as 85, 83, 81 and 83% respectively. Si-nHap particle incorporation slightly decreased the total porosity by enlarging the pore wall surface. Similarly, Lu et al. indicated that the porous structure of n-HA/hydroxypropyl chitosan composite scaffolds did not alter significantly with n-Hap incorporation. However, the pore volume of scaffolds was found to decrease due to the n-HA deposition on the pore walls [36]. The effect of Si-nHap particle dispersion in the chitosan matrix was investigated with SEM and AFM analysis. Porous layers were observed with backscatter mode to determine the distribution of Si-nHap particles in the polymer surface. SEM images indicated that Si-nHap particles were homogeneously distributed in the pore wall surface of both 10% and 50% concentrations (Fig. 5 a,b). In addition, AFM analysis was performed to observe the Si-nHap particle dispersion in the chitosan matrix. AFM images indicated that Si-nHap particle incorporation (20 wt%) in the chitosan matrix altered the surface topography and increased the surface roughness by forming spherical nanopatterns on the polymer surface (Fig. 6). This spherical nanostructure formed by Si-nHap particles induces an increase in surface area of scaffold and protein adsorption. Subsequently, change in surface topography at nano level affects bioactivity by enhancing osteoblast attachment and biomineralization.

3.3. Physical characterization

Mechanical properties of porous nanocomposite layers which were fabricated with low molecular weight and medium molecular weight chitosan were investigated with compression tests. Dry specimens were compressed up to 75% and 90% of initial height with 5 mm/min test speed to investigate the compressibility of scaffolds at the defect site during surgical procedure. Stress-strain curves of LMW chitosan and LMW Chitosan-50% Si-nHap nanocomposite group at 75% and 90% maximum strain is given in supplementary file (Fig. S4). Results indicated that Si-nHap incorporation up to 50% (*w*/w) in the chitosan matrix for both two different strain percentages increased the compression moduli (Fig. 7e,f). However, LMW chitosan groups showed higher moduli results at 90% maximum strain compared to 75%. This increase concludes the positive effect of homogenous Si-nHap dispersion on pore walls of scaffold. Compression modulus of chitosan scaffold was found as 81.4 kPa and increased to 212.5 kPa with 50% Si-nHap incorporation at 90% maximum strain. Lu and co-workers fabricated nano-hydroxyapatite/hydroxypropyl chitosan composite scaffolds and investigated the effects of nanohydroxyapatite incorporation in mechanical characteristics of chitosan matrix. Results indicated that the compressive strength and stiffness were dramatically increased by in-creasing the amount of n-Hap due to the formation of more rigid structures by intramolecular cross-linking of polymer matrix [36].

Water absorption capacity is an important factor for dental membranes to prevent body fluid and blood accumulation at the periodontal

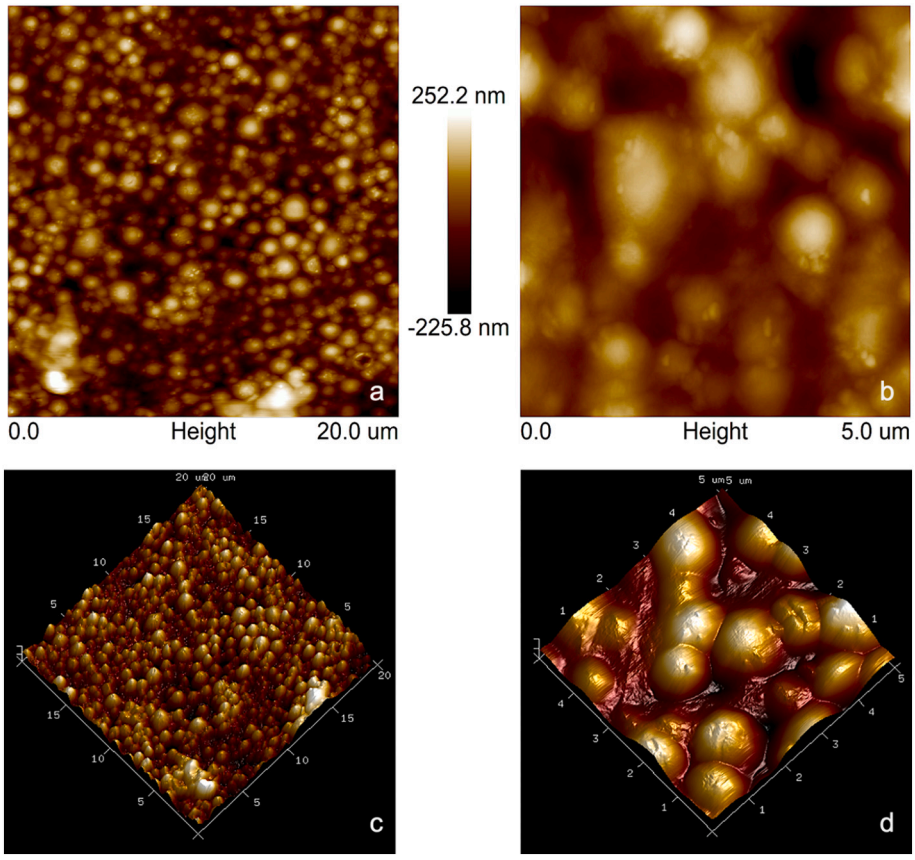

Fig. 6. AFM images of Chitosan-20%Si-nHap composite membranes showing surface topography with height and 3D modes. Phase images of Si-nHap particles are depicted as (a) and (b); surface topography of particle distribution is depicted as (c) and (d) at 20 μm and 5 μm scale, respectively.

defect and to provide effective protein adsorption for cell-material interaction. Thus, swelling capacity of porous layers were investigated in PBS solution for 24–48 h period. Swelling ratio was evaluated with weight change determination after incubation in PBS solution. Results showed that Si-nHap particle incorporation slightly increased the water absorption capacity of the porous layer due to the hydrophilic nature of silica (Fig. 7a). Swelling ratio of LMW chitosan groups increased proportionally with increasing Si-nHap concentration. However, MMW chitosan groups did not show a similar increasing trend in water absorption capacity. Si-nHap incorporation in the chitosan matrix provided enhanced swelling properties at the defect site. Protein adsorption on a biomaterial surface is the first step of cell-material interaction. Cell attachment on a material surface is mainly related with body fluid absorption and protein adsorption. Biomaterial first contacts with body fluid and absorbs the body fluid. This leads to interaction of proteins with the material surface. Then, cells interact with protein bound material surfaces. Thus, BSA adsorption on porous layers were measured for 24–48 h periods to investigate the effect of Si-nHap particles on the polymer surface (Fig. 7b). Protein adsorption results indicated that Si-nHap incorporation induced albumin adsorption on material surface with increasing concentration, and incubation time from 60 μg/ml to 300 μg/ml. Si-nHap particles both altered surface morphology and enhanced water uptake capacity with its hydrophilic character. These factors led to a positive effect on interaction and physical adsorption of proteins on the material surface.

Chitin and chitosan biopolymers can be degraded by two enzymes, chitinase and lysozyme regarding the presence of *N*-acetyl groups and their distribution in the backbone [37]. Therefore, biodegradation study was carried out in the presence of lysozyme to mimic the biomaterial-blood interaction at the defect site. Biodegradation of composites were evaluated with weight loss % at different incubation periods. Results indicated that weight loss percentages of all groups were found similar at the 7th day of incubation (Fig. 7c). However, on 21 and 28 days, Si-nHap incorporation decreased the biodegradation rate and chitosan/Si-nHap scaffolds showed lower total % weight loss up to 28 days. At the end of 28 days, chitosan scaffolds lost 79% of initial weight whereas chitosan- 50%Si-nHap composite scaffolds lost 50% of initial weight. In literature, similar results were indicated as the n-Hap addition to chitosan matrix decrease the degradation rate and changing the n-Hap amount could alter the degradation profile in controlled way [36]. Ressler and co-workers also fabricated chitosan-Hap hydrogels and investigated the degradation behavior of composite hydrogels with different lysozyme concentrations. They found that hydrogel composites are highly stable for 28 days, even in extreme conditions with much higher concentration of lysozyme than physiological conditions. [38].

The open porosity of LMW chitosan groups was investigated with liquid displacement method. Chitosan/Si-nHap composites possessed highly connected porous structure with open porosity range of 73–80% (Fig. 7d). Si-nHap particles did not show any effect on porosity of scaffolds up to 50% concentration. At maximum concentration as 50%, Si-nHap incorporation slightly decreased the porosity of chitosan scaffold to 73% due to the possible alterations on pore wall architecture as enlargement of surface area.

3.4. Antimicrobial activity

Dental tissue regeneration generally requires contamination control due to the possible trauma or defect that causes dentin loss. Therefore, the prevention of possible infection at the defect site is important for tissue regeneration by using biomaterials with antimicrobial property [39].

The antimicrobial activities of scaffold forming solutions of

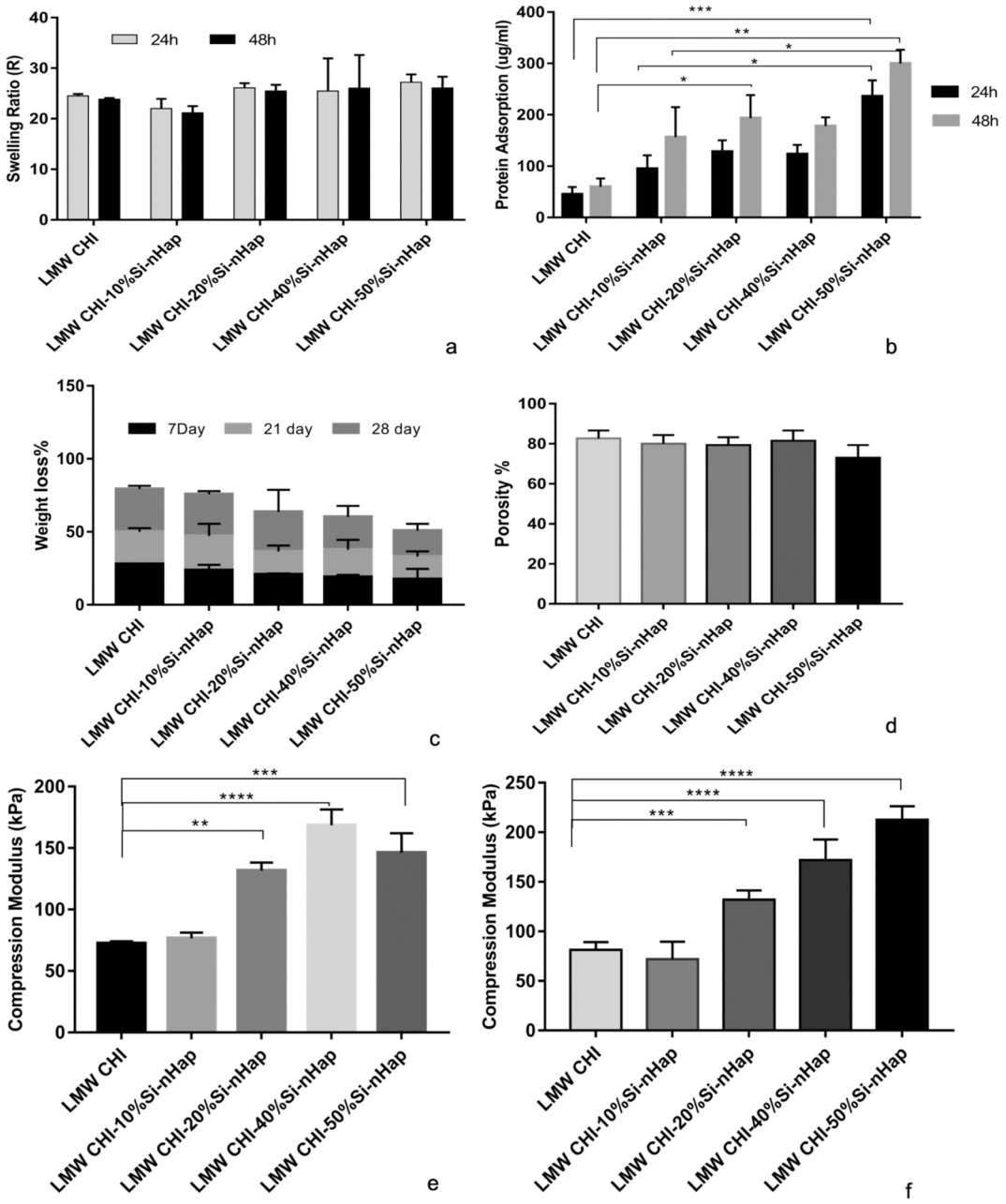

Fig. 7. Physical characteristics of bilayer chitosan/Si-nHap nanocomposite membranes: Water absorption capacity (a); Protein adsorption (b); Weight loss% (c) and Open porosity % (d); Compression moduli of LMW chitosan/Si-nHap nanocomposites at 75% and 90% strain, respectively (e,f).

Table 1
Inhibition zones of chitosan/Si-nHap nanocomposites against *E. coli* and *S. aureus*.

Inhibition zone diameter (mm)	*E. coli* (Gram negative)	*S. aureus* (Gram positive)
Chitosan	0,1 (<1)	0,1 (<1)
Chitosan-10%Si-nHap	1,51	1,00
Chitosan-20%Si-nHap	1,50	1,28
Chitosan-40%Si-nHap	1,25	1,00
Chitosan-50%Si-nHap	1,83	1,50

chitosan/Si-nHap groups were investigated by using disc diffusion and tube dilution methods against gram-negative *E. coli* and gram-positive *S. aureus*. It is known that *E. coli* and *S. aureus* are mostly observed pathogenic bacteria at the wound site. Thus, these bacteria were used to determine the inhibition effect of Si-nHap particles at wound area. Table 1 shows the antibacterial zones of chitosan/Si-nHap nanocomposites cultivated with pathogens for 24 h. Tube dilution assay results showed that chitosan/Si-nHap composite solutions inhibited the colony formation whereas control groups of *E. coli* and *S. aureus* were obtained as colonies covering all over the surface of petri dishes (Fig. 8). Concerning the colony formation, chitosan/Si-nHap composites showed a significant inhibiting effect on gram negative *E. coli* whereas, weak inhibiting effect against *S. aureus* colonies. Colony numbers of *E. coli* and *S. aureus* counted on petri dishes for each group were depicted in Table 2. Colony counting results also indicated that chitosan/Si-nHap composite solutions showed a significant decreasing effect on *E. coli* colonies compared to *S. aureus* colonies. Qualitative and quantitative results showed that 40% and 50% Si-nHap incorporated chitosan scaffolds inhibited both gram negative and positive bacteria effectively. In literature, chitosan is known to inhibit some Gram-negative and Gram-

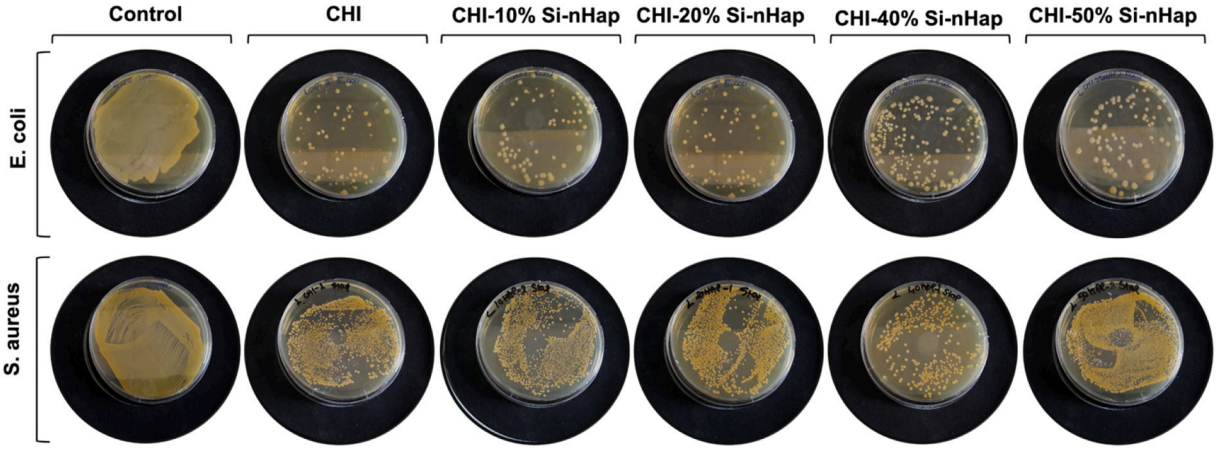

Fig. 8. Tube dilution method: colony formation with chitosan/Si-nHap solutions after 24 h of incubation.

Table 2
Colony numbers of tube dilution groups counted after 24 h of cultivation on agar.

Groups	Colony number	
	E. coli	*S. aureus*
Negative control	$>10^5$	$>10^5$
Chitosan	59	$<10^5$
Chitosan-10%Si-nHap	78	1500
Chitosan-20%Si-nHap	20	$<10^5$
Chitosan-40%Si-nHap	188	227
Chitosan-50%Si-nHap	110	$<10^5$

positive bacteria such as *Actinobacillus actinomycetemcomitans* and *Streptococcus mutans*, thus it is considered as a good biopolymer source as biomaterial in maxillofacial GBR applications. In addition, chitosan shows synergistical antibacterial affect when blended with other biopolymers [40]. In literature, Sutha and co-workers investigated the antimicrobial activity of silicon integrated hydroxyapatite/chitosan composite coated on stainless steel implants. Results indicated that increasing Si concentration enhanced the antimicrobial activity by increasing zone diameters for both *E. coli* and *S. aureus*. This antimicrobial effect was correlated with variation in surface charges due to the presence of Si ions [41]. (See Fig. 8).

3.5. In vitro studies

In vitro studies were performed with Saos-2 and NIH/3T3 cell lines to mimic each layer of the periodontal defect to provide microenvironment for periodontal regeneration as well as preventing the migration of fibroblasts to the defect site and limiting their proliferation. Saos-2 cells were seeded on porous chitosan/Si-nHap composite layer whereas, NIH/3T3 cells were seeded on chitosan/PEO nanofiber layer to investigate the cytocompatibility of each layer.

3.5.1. Cell attachment and spreading

Cell attachment and spreading on biomaterial surfaces are major factors to induce cell bioactivity for proliferation and differentiation. Favorable cell-material surface interactions which induce cell attachment and spreading, can stimulate intracellular tension and promote the osteogenesis by upregulating the expression of specific markers as runt-related transcription factor 2 (RUNX2), bone morphogenetic protein 2 (BMP2) and osteocalcin [42,43]. In bone tissue, osteoblasts interact with material surfaces with respect to surface characteristics as topography, chemistry or surface energy. These characteristics significantly affect the protein adsorption that initiates the cell adhesion for proliferation, differentiation and biomineralization in bone tissue formation. [43,44]. Saos-2 cell attachment was investigated at the 7th day of incubation to observe the effect of Si-nHap dispersion on cell-material surface interaction. Si doped nanohydroxyapatite particles altered the surface morphology as indicated in AFM results (Fig. 6) and dispersed on chitosan matrix surface as shown in SEM images (Fig. 5). Thus, Si doped nanohydroxyapatite particles enhanced osteoblast attachment on scaffold surfaces with their hydrophilic structure and spherical morphology altering the surface roughness. Fluorescence microscopy images showed that Saos-2 cells attached with filopodia as cytoplasmic elongations on pore wall surfaces and proliferated successfully on porous structure due to the inducing effect of Si doped nanohydroxyapatite particles which distributed on material surface (Fig. 9). In literature it is indicated that calcium silicate cements with a higher Si content promoted cell attachment and triggered total integrin, pFAK and COL I expression. Botelho and co-workers also reported that Si-Hap showed different surface properties, with more negative surface charge and induced protein adsorption leading to higher cell adhesion and consequent proliferation. In another study, Kalia and co-workers investigated the silicon-substituted hydroxyapatite coating on osteoblast attachment and revealed that Si nanoparticles changed the surface properties of hydroxyapatite by altering wettability and surface roughness. Results showed that these changes enhanced the osteoblast adhesion [24,45,46].

3.5.2. Cell proliferation

Cell proliferation on each layer was investigated with WST-1 assay. Saos-2 cells were inoculated with a density of 10^6 cells/ml and incubated on a porous layer for 28 days. NIH/3T3 cells were seeded with a density of 10^6 cells/ml on nanofiber layer (1x1cm) and incubated for 28 days. Results indicated that osteoblastic Saos-2 cells highly proliferated on porous chitosan/Si-nHap composite layers up to 28 days (Fig. 10a). However, Saos-2 cell proliferation is slightly higher on chitosan scaffold compared to nanocomposite groups. This may arise from the possible osteoblastic activity and differentiation of Saos-2 cells instead of proliferation. NIH/3T3 cell proliferation was found highest on the 7th day of incubation. NIH/3T3 proliferation decreased with the incubation time due to the barrier effect of chitosan/PEO nanofiber layer (Fig. 10 b). NIH/3T3 fibroblast cells were incubated with high cell density on the chitosan/PEO nanofiber layer to mimic the excessive fibroblast migration at the dental defect during the healing process. Thus, proliferation decreased after 7 days of incubation with the barrier effect of nanofiber structure and high confluency of fibroblasts on nanofiber surfaces.

3.5.3. ALP activity, osteocalcin secretion and hydroxyproline content

Alkaline phosphatase is an early differentiation marker which is known to increase the local concentration of inorganic phosphate for

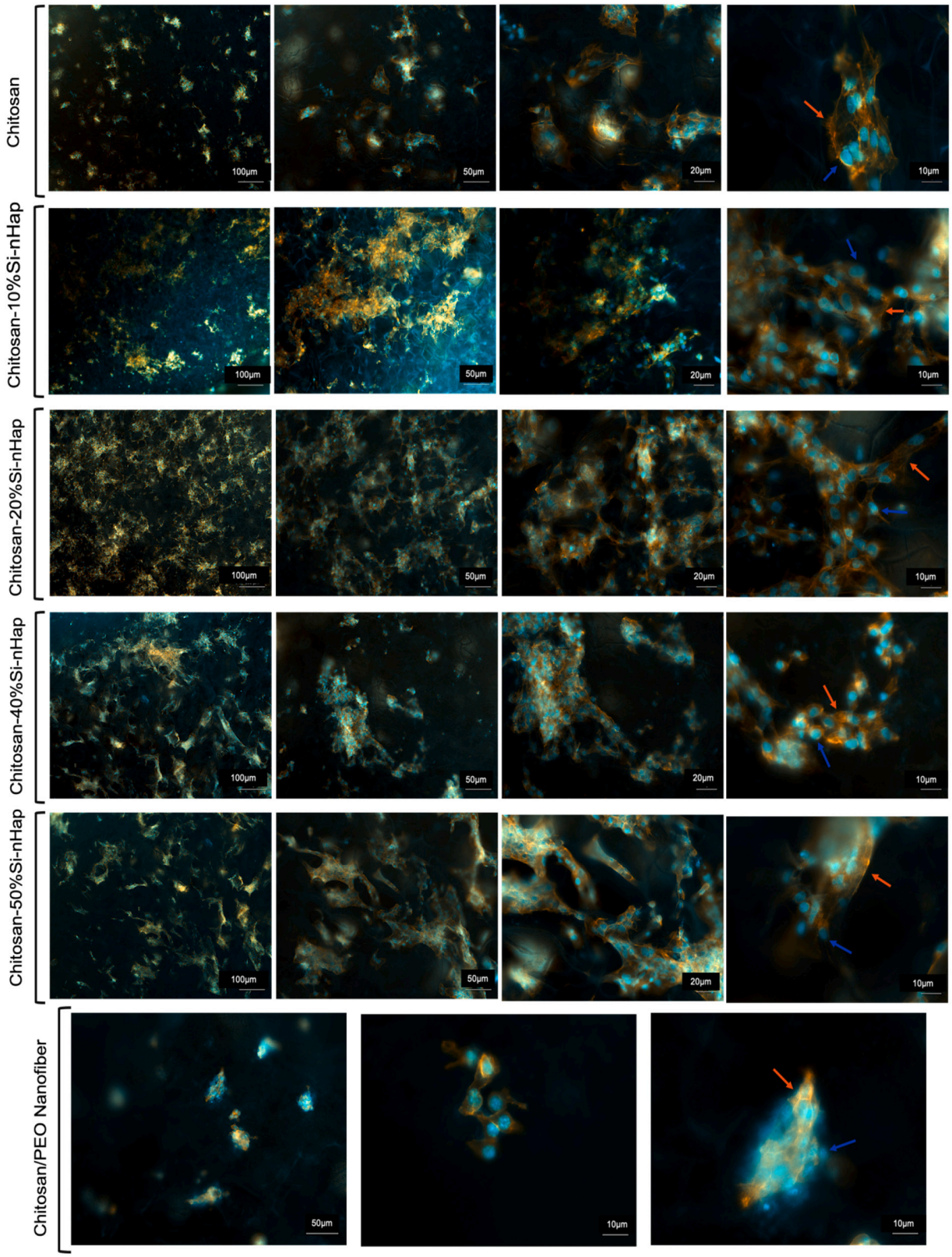

Fig. 9. Fluorescence images of Saos-2 and NIH/3T3 attachment on chitosan/Si-nHap porous layers and Chitosan/PEO nanofiber layer at 100 μm, 50 μm, 20 μm and 10 μm scale respectively.

biomineralization. ALP activity of Saos-2 cells on the chitosan/Si-nHap porous layer was investigated for 28 days to investigate the bioactivity before biomineralization. Saos-2 cells possess a mature osteoblast phenotype, with high biomineralization capacity and showed higher ALP activity than other osteosarcoma cell lines. In literature, Saos-2 cells are found to show similar ALP activity levels compared to human primary osteoblast cells at the early incubation time, but 120-fold higher ALP activity was observed after 14 days of incubation. Consequently,

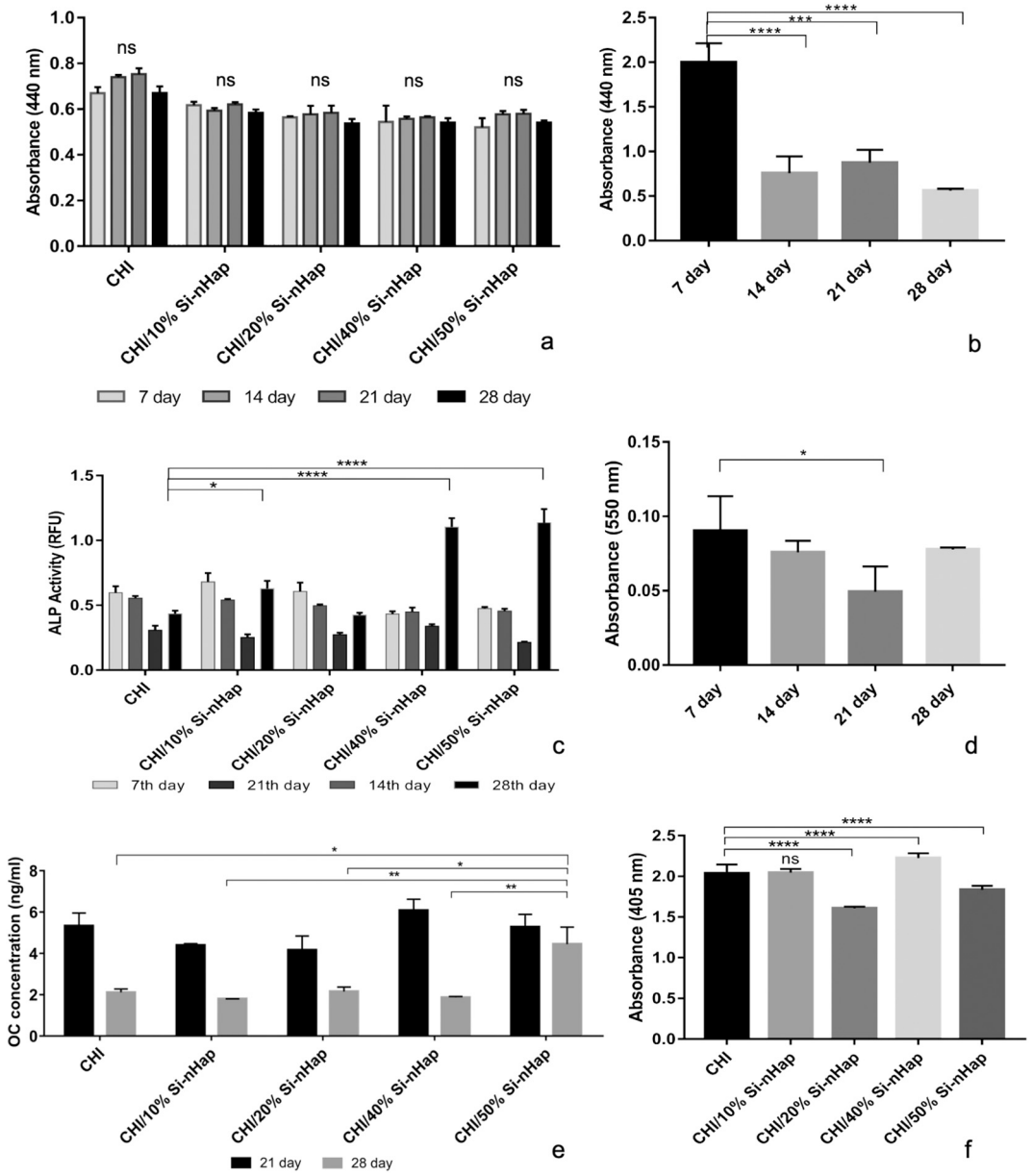

Fig. 10. *In vitro* bioactivity of Saos-2 and NIH/3 T3 cells on porous and nanofiber layers: Saos-2 proliferation (a), NIH/3T3 proliferation (b), ALP activity of Saos-2 cells (c), Hydroxyproline content of NIH/3T3 cells (d) Osteocalcin secretion (21–28 day) and calcium deposition determination with ARS extraction of Saos-2 cells at 28th day (e,f).

SaOs-2 cells show responses resembling human osteoblasts (hFob) more closely, with regard to osteoblastic marker expression [47–49]. All groups showed similar ALP secretion trends during incubation (Fig. 10 c). Nanocomposite scaffolds with higher Si-nHap ratio (40 and 50%) ALP secretion were found slightly lower at 7 and 14 days of incubation. However, on the 28th day highest ALP levels were observed for 40% and 50% Si-nHap loaded groups. This may result from the Si-nHap particle distribution on the chitosan matrix surface. Hence, the osteogenic differentiation is strongly related with topography and roughness of the biomaterial surface that osteoblasts attach to. Particle size and distribution on composite material surfaces are important factors that alter the surface topography and enhance osteoblast-material interaction in bone regeneration [50]. Si-nHap particles loaded in the chitosan matrix at high ratio (40 and 50%) constituted a different surface pattern compared to control group and nanocomposite groups with low Si-nHap ratio. This surface morphology change was indicated with SEM and AFM analyses (Figs. 5 & 6). Hence ALP activity of Saos-2 cells cultivated on a porous layer surface was significantly induced.

Hydroxyproline (HP) is a non-essential amino acid that is found in collagen and specific to collagenous fiber in connective tissue. Thus, HP secretion of NIH/3T3 fibroblasts were measured during proliferation study to determine the collagen secretion. Results indicated that HP secretion levels were found higher at early days of incubation (7–14 days). Hp secretion levels showed similar trend with fibroblast proliferation and indicated that fibroblast proliferation was limited with the barrier properties of nanofiber layer (Fig. 10 d).

Dentin and enamel synthesis process is initiated by the mineral production of ameloblasts and odontoblasts on the surface of organic matrix. In the biomineralization process non-collagenous proteins play a significant role to induce the calcium deposition and subsequently hydroxyapatite crystal growth [39]. Osteocalcin (OC) is the most abundant non-collagenous g-carboxyglutamate protein in the bone matrix and expressed by osteoblasts in the late stage of their differentiation. Osteocalcin provides a strong binding affinity for the Hap and functions

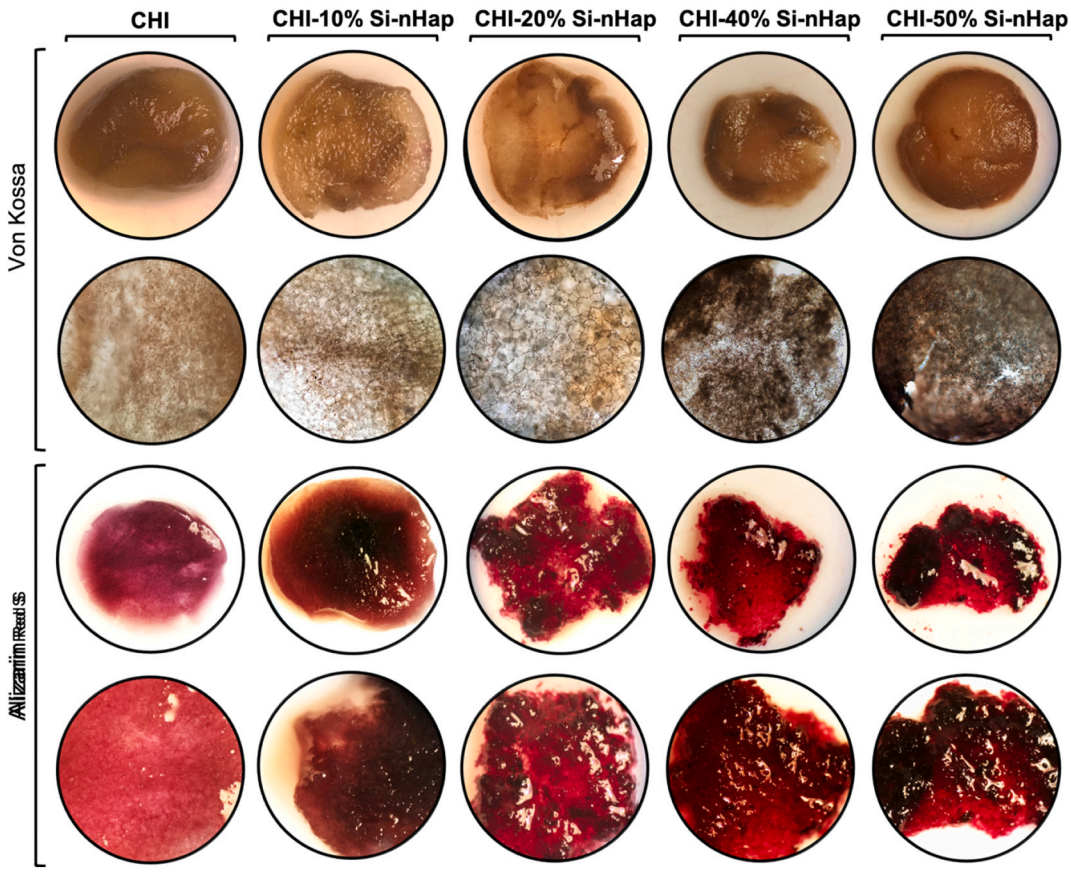

Fig. 11. Biomineralization on scaffolds is depicted with the stereo-images of von Kossa (2×, 10× magnification) and Alizarin Red S (2×, 4× magnification) stained CHI/Si-nHap scaffolds on the 28th day. (For interpretation of the references to colour in this figure legend, the reader is referred to the web version of this article.)

with osteopontin (OPN) to mediate bonding at HAp mineral to mineral interfaces in the extrafibrillar space. By this way, OC regulates the mineralization process in bone regeneration [51,52]. Osteocalcin secretion level of Saos-2 cells was investigated for the late term of osteoblast bioactivity (Fig. 10 e). Results indicated that Si-nHap incorporation at high concentrations (40–50%) induced the biomineralization at 21 days of incubation. In addition, osteocalcin secretion of Saos-2 cells was found significantly higher on 50% Si-nHap incorporated scaffolds on the 28th day.

3.5.4. *Biomineralization on scaffold surface*

Biomineralization on the material surface was also determined as Ca—P deposition and visualized with Alizarin Red S and von Kossa staining at the end of cell cultivation (Fig. 11). Stereo images of von Kossa stained scaffolds showed phosphate accumulation on material surface as dark brown zones and indicated that Si-nHap incorporation enhanced the phosphate deposition on material surface with increasing concentrations. At high Si-nHap concentrations (40–50%) phosphate deposition was observed homogeneously where heterogeneous zones were obtained at low Si-nHap incorporated groups. This non-heterogeneous distribution may arise from the Si-nHap particle dispersion on the surface. Stereo-images of Alizarin Red S staining of scaffolds showed the calcium nucleation and deposition as dark red accumulations on the material surface. Images indicated that Si-nHap particle incorporation induced the calcium deposition on scaffold surface when compared to chitosan scaffold. Consequently, these staining methods showed that significant mineral deposition was observed on nanocomposite groups compared to control chitosan scaffold. However, both of the two staining methods did not indicate the mineral deposition difference between nanocomposite groups. Thus, Alizarin Red S stain was extracted and measured spectrophotometrically to obtain semi-quantitative results and indicate the difference between groups. Absorbance results indicated that maximum calcium deposition was observed on chitosan-40% Si-nHap group. In a study, osteogenic effect of n-Hap particle incorporation in hydroxypropyl chitosan matrix was investigated with Alizarin Red S staining. It was found that n-Hap addition enhanced the biomineralization capacity of by inducing calcium deposition [36]. Kermani and co-workers investigated the biological effects of Si doped calcium phosphates on biomineralization with alizarin red staining and quantified the difference of calcium deposition spectrophotometrically. Results showed that Si doped groups induced the calcium nodule formation [50].

4. Conclusion

In this study, novel bilayer design was obtained with the integration of biopolymer based nanocomposite microporous and nanofiber layers to form bioactive GBR membrane for periodontal applications. Chitosan/Si-nHap and Chitosan/PEO based bilayer nanocomposite membranes were fabricated successfully with freeze-drying and electrospinning to form integrated two different layers having distinct morphology. The porous layer was obtained with high porosity in a range of 81–85% with average pore size range 177–191 μm which is appropriate for cell proliferation. The nanofiber layer was obtained with an average fiber diameter 107 nm to show barrier properties to prevent fibroblast migration to the defect site. Two layers were successfully integrated during the fabrication process. Si-nHap incorporation to a porous layer of membrane induced the physical properties of the material by enhancing compression modulus, protein adsorption and controlling biodegradation rate with increasing concentrations. Antimicrobial tests indicated that 40% and 50% Si-nHap incorporated chitosan scaffolds inhibited both gram negative and positive bacteria

effectively. *In vitro* cell culture studies showed that Si-nHap incorporated porous layers increased cell attachment and spreading. Besides, Si-nHap particles induced ALP activity, OC secretion and biomineralization at high concentrations. The nanofiber layer also showed barrier effects on fibroblast activity by preventing cell proliferation during 28 day of incubation and decreasing hydroxyproline level as a biomarker for ECM formation in soft tissue formation. Consequently, bilayer guided tissue membranes showed inducing effect for osteoblast bioactivity with its porous nanocomposite layer and barrier effect for undesired fibroblast proliferation at the defect site during the healing process.

Declaration of competing interest

The authors declare that they have no known competing financial interests or personal relationships that could have appeared to influence the work reported in this paper.

Acknowledgments

This work was financed by the Ministry of Industry and Technology SAN-TEZ Industrial Thesis Project (0494.STZ.2013-2). Authors are grateful to Assist. Prof. Dr. Meltem ALPER from Aksaray University for supplying Saos-2 cell line. Authors thank to Biotechnology and Bioengineering Research and Application Center (IZTECH BIOMER), Center for Materials Research (IZTECH CMR) in Izmir Institute of Technology (IZTECH) for fluorescence microscopy, antimicrobial tests, SEM, AFM and stereomicroscopy analyses. Authors are also grateful to the Central Research Test and Analysis Laboratory Application and Research Center in Ege University for micro-CT analyses.

Appendix A. Supplementary data

Supplementary data to this article can be found online at https://doi.org/10.1016/j.msec.2021.112298.

References

[1] G. Polimeni, A. V. Xiropaidis, U.M.E. Wikesjö, Biology and principles of periodontal wound healing/regeneration, Periodontol. 2000. 41 (2006) 30–47. doi: https://doi.org/10.1111/j.1600-0757.2006.00157.x.
[2] L. Shue, Z. Yufeng, U. Mony, Biomaterials for periodontal regeneration: a review of ceramics and polymers, Biomatter. 2 (2012) 271–277, https://doi.org/10.4161/biom.22948.
[3] M. Lian, B. Sun, Z. Qiao, K. Zhao, X. Zhou, Q. Zhang, D. Zou, C. He, X. Zhang, Bilayered electrospun nanofibrous membrane with osteogenic and antibacterial properties for guided bone regeneration, Colloids Surf. B Biointerfaces 176 (2019) 219–229, https://doi.org/10.1016/j.colsurfb.2018.12.071.
[4] V.I. dos Santos, C. Merlini, Á. Aragones, K. Cesca, M.C. Fredel, In vitro evaluation of bilayer membranes of PLGA/hydroxyapatite/β-tricalcium phosphate for guided bone regeneration, Mater. Sci. Eng. C 112 (2020), 110849, https://doi.org/10.1016/j.msec.2020.110849.
[5] G.L. Abe, J.I. Sasaki, C. Katata, T. Kohno, R. Tsuboi, H. Kitagawa, S. Imazato, Fabrication of novel poly(lactic acid/caprolactone) bilayer membrane for GBR application, Dent, Mater. 36 (2020) 626–634, https://doi.org/10.1016/j.dental.2020.03.013.
[6] J. Liu, D.G. Kerns, Mechanisms of guided bone regeneration, a review, Open Dent. J. 8 (2014) 56–65, https://doi.org/10.2174/1874210601408010056.
[7] R. IA, S. GS, F. AE, G. CJ, S. SH, E. JA, G. MS, B. GL, Barrier membranes for dental applications: a review and sweet advancement in membrane developments, Mouth and Teeth. 2 (2018) 1–9. doi:10.15761/mtj.1000108.
[8] T. Fernandez-medina, A. Nanda, Regenerative approaches in dentistry, Regen, Approaches Dent. (2021), https://doi.org/10.1007/978-3-030-59809-9.
[9] P. Gentile, V. Chiono, C. Tonda-Turo, A.M. Ferreira, G. Ciardelli, Polymeric membranes for guided bone regeneration, Biotechnol. J. 6 (2011) 1187–1197, https://doi.org/10.1002/biot.201100294.
[10] W. Florjanski, S. Orzeszek, A. Olchowy, N. Grychowska, W. Wieckiewicz, A. Malysa, J. Smardz, M. Wieckiewicz, Modifications of polymeric membranes used in guided tissue and bone regeneration, Polymers (Basel). 11 (2019) 1–11, https://doi.org/10.3390/polym11050782.
[11] S. Ramesh, L. Lungaro, D. Tsikritsis, E. Weflen, I.V. Rivero, A.P.D. Elfick, Fabrication and evaluation of poly(lactic acid), chitosan, and tricalcium phosphate biocomposites for guided bone regeneration, J. Appl. Polym. Sci. 135 (2018) 1–10, https://doi.org/10.1002/app.46692.
[12] F. Sharif, S. Tabassum, W. Mustafa, A. Asif, F. Zarif, M. Tariq, S.A. Siddiqui, M. A. Gilani, I. Ur Rehman, S. MacNeil, Bioresorbable antibacterial PCL-PLA-nHA composite membranes for oral and maxillofacial defects, Polym. Compos. 40 (2019) 1564–1575, https://doi.org/10.1002/pc.24899.
[13] S.C. Santos, K.G. Spaniol, N.E. Chaves-Silva, R.P.M. Fernandes, D.S. Tavares, W. Acchar, E.A. dos Santos, Copper-containing bioactive glass/PVA membranes for guided bone regeneration, J. Non Cryst. Solids 557 (2021), https://doi.org/10.1016/j.jnoncrysol.2020.120628.
[14] D. Zhao, T. Zhu, J. Li, L. Cui, Z. Zhang, X. Zhuang, J. Ding, Poly(lactic-co-glycolic acid)-based composite bone-substitute materials, Bioact. Mater. 6 (2021) 346–360, https://doi.org/10.1016/j.bioactmat.2020.08.016.
[15] R. Dimitriou, G.I. Mataliotakis, G.M. Calori, P.V. Giannoudis, The role of barrier membranes for guided bone regeneration and restoration of large bone defects: current experimental and clinical evidence, BMC Med. 10 (2012) 81, https://doi.org/10.1186/1741-7015-10-81.
[16] S. Ahmed, A. Ali Annu, J. Sheikh, A review on chitosan centred scaffolds and their applications in tissue engineering, Int. J. Biol. Macromol. 116 (2018) 849–862, https://doi.org/10.1016/j.ijbiomac.2018.04.176.
[17] A. Ali, S. Ahmed, A review on chitosan and its nanocomposites in drug delivery, Int. J. Biol. Macromol. 109 (2018) 273–286, https://doi.org/10.1016/j.ijbiomac.2017.12.078.
[18] E. Fakhri, H. Eslami, P. Maroufi, F. Pakdel, S. Taghizadeh, K. Ganbarov, M. Yousefi, A. Tanomand, B. Yousefi, S. Mahmoudi, H.S. Kafil, Chitosan biomaterials application in dentistry, Int. J. Biol. Macromol. 162 (2020) 956–974, https://doi.org/10.1016/j.ijbiomac.2020.06.211.
[19] A.Z. Alshemary, M. Akram, Y.F. Goh, U. Tariq, F.K. Butt, A. Abdolahi, R. Hussain, Synthesis, characterization, in vitro bioactivity and antimicrobial activity of magnesium and nickel doped silicate hydroxyapatite, Ceram. Int. 41 (2015) 11886–11898, https://doi.org/10.1016/j.ceramint.2015.06.003.
[20] A.M. Pietak, J.W. Reid, M.J. Stott, M. Sayer, Silicon substitution in the calcium phosphate bioceramics, Biomaterials. 28 (2007) 4023–4032, https://doi.org/10.1016/j.biomaterials.2007.05.003.
[21] E.S. Thian, J. Huang, S.M. Best, Z.H. Barber, W. Bonfield, Magnetron co-sputtered silicon-containing hydroxyapatite thin films - an in vitro study, Biomaterials. 26 (2005) 2947–2956, https://doi.org/10.1016/j.biomaterials.2004.07.058.
[22] M. Bohner, Silicon-substituted calcium phosphates - a critical view, Biomaterials. 30 (2009) 6403–6406, https://doi.org/10.1016/j.biomaterials.2009.08.007.
[23] Z.Y. Qiu, I.S. Noh, S.M. Zhang, Silicate-doped hydroxyapatite and its promotive effect on bone mineralization, Front, Mater. Sci. Forum 7 (2013) 40–50, https://doi.org/10.1007/s11706-013-0193-9.
[24] P. Kalia, R.A. Brooks, S.D. Kinrade, D.J. Morgan, A.P. Brown, N. Rushton, R. Jugdaohsingh, Adsorption of amorphous silica nanoparticles onto hydroxyapatite surfaces differentially alters surfaces properties and adhesion of human osteoblast cells, PLoS One 11 (2016) 1–15, https://doi.org/10.1371/journal.pone.0144780.
[25] Y. Huang, Z. Xu, X. Zhang, X. Chang, X. Zhang, Y.C. Li, T. Ye, R. Han, S. Han, Y. Gao, X. Du, H. Yang, Nanotube-formed Ti substrates coated with silicate/silver co-doped hydroxyapatite as prospective materials for bone implants, J. Alloys Compd. 697 (2017) 182–199, https://doi.org/10.1016/j.jallcom.2016.12.139.
[26] S.S. Bin Qasim, M.S. Zafar, F.H. Niazi, M. Alshahwan, H. Omar, U. Daood, Functionally graded biomimetic biomaterials in dentistry: an evidence-based update, J. Biomater. Sci. Polym. Ed. 31 (2020) 1144–1162, https://doi.org/10.1080/09205063.2020.1744289.
[27] M. Masoudi Rad, S. Nouri Khorasani, L. Ghasemi-Mobarakeh, M.P. Prabhakaran, M.R. Foroughi, M. Kharaziha, N. Saadatkish, S. Ramakrishna, Fabrication and characterization of two-layered nanofibrous membrane for guided bone and tissue regeneration application, Mater. Sci. Eng. C 80 (2017) 75–87, https://doi.org/10.1016/j.msec.2017.05.125.
[28] E.M. Varoni, S. Vijayakumar, E. Canciani, A. Cochis, L. De Nardo, G. Lodi, L. Rimondini, M. Cerruti, Chitosan-based trilayer scaffold for multitissue periodontal regeneration, J. Dent. Res. 97 (2018) 303–311, https://doi.org/10.1177/0022034517736255.
[29] M.H. Ho, C.C. Hsieh, S.W. Hsiao, D. Van Hong Thien, Fabrication of asymmetric chitosan GTR membranes for the treatment of periodontal disease, Carbohydr, Polym. 79 (2010) 955–963, https://doi.org/10.1016/j.carbpol.2009.10.031.
[30] T. Freier, H.S. Koh, K. Kazazian, M.S. Shoichet, Controlling cell adhesion and degradation of chitosan films by N-acetylation, Biomaterials. 26 (2005) 5872–5878, https://doi.org/10.1016/j.biomaterials.2005.02.033.
[31] G. Toskas, C. Cherif, R.D. Hund, E. Laourine, B. Mahltig, A. Fahmi, C. Heinemann, T. Hanke, Chitosan(PEO)/silica hybrid nanofibers as a potential biomaterial for bone regeneration, Carbohydr, Polym. 94 (2013) 713–722, https://doi.org/10.1016/j.carbpol.2013.01.068.
[32] S.B. Qasim, S. Najeeb, R.M. Delaine-Smith, A. Rawlinson, I. Ur Rehman, Potential of electrospun chitosan fibers as a surface layer in functionally graded GTR membrane for periodontal regeneration, Dent, Mater. 33 (2017) 71–83, https://doi.org/10.1016/j.dental.2016.10.003.
[33] D.W. Hutmacher, J.T. Schantz, C.X.F. Lam, K.C. Tan, T.C. Lim, State of the art and future directions of scaffold-based bone engineering from a biomaterials perspective, J. Tissue Eng. Regen. Med. (2007), https://doi.org/10.1002/term.24.
[34] T.G. Kim, H.J. Chung, T.G. Park, Macroporous and nanofibrous hyaluronic acid/collagen hybrid scaffold fabricated by concurrent electrospinning and deposition/leaching of salt particles, Acta Biomater. 4 (2008) 1611–1619, https://doi.org/10.1016/j.actbio.2008.06.008.
[35] J.L. Lowery, N. Datta, G.C. Rutledge, Effect of fiber diameter, pore size and seeding method on growth of human dermal fibroblasts in electrospun poly (ε-caprolactone) fibrous mats, Biomaterials. 31 (2010) 491–504, https://doi.org/10.1016/j.biomaterials.2009.09.072.

[36] H.T. Lu, T.W. Lu, C.H. Chen, F.L. Mi, Development of genipin-crosslinked and fucoidan-adsorbed nano-hydroxyapatite/hydroxypropyl chitosan composite scaffolds for bone tissue engineering, Int. J. Biol. Macromol. 128 (2019) 973–984, https://doi.org/10.1016/j.ijbiomac.2019.02.010.
[37] K.Y. Lee, W.S. Ha, W.H. Park, Blood compatibility and biodegradability of partially N-acylated chitosan derivatives, Biomaterials. 16 (1995) 1211–1216, https://doi.org/10.1016/0142-9612(95)98126-Y.
[38] A. Ressler, J. Ródenas-Rochina, M. Ivanković, H. Ivanković, A. Rogina, G. Gallego Ferrer, Injectable chitosan-hydroxyapatite hydrogels promote the osteogenic differentiation of mesenchymal stem cells, Carbohydr, Polym. 197 (2018) 469–477, https://doi.org/10.1016/j.carbpol.2018.06.029.
[39] K.M. Galler, R.N. D'Souza, J.D. Hartgerink, G. Schmalz, Scaffolds for dental pulp tissue engineering., Adv, Dent. Res. 23 (2011) 333–339, https://doi.org/10.1177/0022034511405326.
[40] M. Martín-Del-campo, D. Fernández-Villa, G. Cabrera-Rueda, L. Rojo, Antibacterial bio-based polymers for cranio-maxillofacial regeneration applications, Appl. Sci. 10 (2020) 1–23, https://doi.org/10.3390/app10238371.
[41] S. Sutha, K. Kavitha, G. Karunakaran, V. Rajendran, In-vitro bioactivity, biocorrosion and antibacterial activity of silicon integrated hydroxyapatite/chitosan composite coating on 316 L stainless steel implants, Mater. Sci. Eng. A C. 33 (2013) 4046–4054, https://doi.org/10.1016/j.msec.2013.05.047.
[42] J.W. Cassidy, J.N. Roberts, C.A. Smith, M. Robertson, K. White, M.J. Biggs, R.O. C. Oreffo, M.J. Dalby, Osteogenic lineage restriction by osteoprogenitors cultured on nanometric grooved surfaces: the role of focal adhesion maturation, Acta Biomater. 10 (2014) 651–660, https://doi.org/10.1016/j.actbio.2013.11.008.
[43] X. Yang, Y. Li, X. Liu, Q. Huang, R. Zhang, Q. Feng, Incorporation of silica nanoparticles to PLGA electrospun fibers for osteogenic differentiation of human osteoblast-like cells, Regen, Biomater. 5 (2018) 229–238, https://doi.org/10.1093/rb/rby014.
[44] K. Anselme, Osteoblast adhesion on biomaterials, Biomaterials. 21 (2000) 667–681, https://doi.org/10.1016/S0142-9612(99)00242-2.
[45] M.Y. Shie, S.J. Ding, Integrin binding and MAPK signal pathways in primary cell responses to surface chemistry of calcium silicate cements, Biomaterials. 34 (2013) 6589–6606, https://doi.org/10.1016/j.biomaterials.2013.05.075.
[46] C.M. Botelho, R.A. Brooks, S.M. Best, M.A. Lopes, J.D. Santos, N. Rushton, W. Bonfield, Human osteoblast response to silicon-substituted hydroxyapatite, J. Biomed. Mater. Res. Part A. 79 (2006) 723–730, https://doi.org/10.1002/jbm.a.
[47] E. Murray, D. Provvedini, D. Curran, B. Catherwood, H. Sussman, S. Manolagas, Characterization of a human osteoblastic osteosarcoma cell line (SAOS-2) with high bone alkaline phosphatase activity, J. Bone Miner. Res. (1987), https://doi.org/10.1002/jbmr.5650020310.
[48] L. Saldaña, F. Bensiamar, A. Boré, N. Vilaboa, In search of representative models of human bone-forming cells for cytocompatibility studies, Acta Biomater. 7 (2011) 4210–4221, https://doi.org/10.1016/j.actbio.2011.07.019.
[49] E.M. Czekanska, In search of an osteoblast cell model for 24 (2012) 1–17.
[50] S.W. Ha, M. Viggeswarapu, M.M. Habib, G.R. Beck, Bioactive effects of silica nanoparticles on bone cells are size, surface, and composition dependent, Acta Biomater. 82 (2018) 184–196, https://doi.org/10.1016/j.actbio.2018.10.018.
[51] A. Neve, A. Corrado, F.P. Cantatore, Osteocalcin: skeletal and extra-skeletal effects, J. Cell. Physiol. 228 (2013) 1149–1153, https://doi.org/10.1002/jcp.24278.
[52] M. Tavakol, T.J. Vaughan, The structural role of osteocalcin in bone biomechanics and its alteration in Type-2 diabetes, Sci, Rep. 10 (2020) 1–10, https://doi.org/10.1038/s41598-020-73141-w.